

## Magnon gap tuning in lithium-doped MnTe

George Yumnam<sup>1,\*</sup>, Duncan H. Moseley<sup>1</sup>, Joseph A. M. Paddison<sup>1</sup>, Christiana Z. Suggs<sup>2</sup>, Emma Zappala<sup>2</sup>, David S. Parker<sup>1</sup>, Garrett E. Granroth<sup>3</sup>, Gerald D. Morris<sup>4</sup>, Md Mobarak Hossain Polash<sup>5</sup>, Daryoosh Vashaei<sup>5</sup>, Michael A. McGuire<sup>1</sup>, Huaizhou Zhao<sup>6</sup>, Michael E. Manley<sup>1</sup>, Benjamin A. Frandsen<sup>2</sup> and Raphaël P. Hermann<sup>1,†</sup>

<sup>1</sup>Materials Science and Technology Division, Oak Ridge National Laboratory, Oak Ridge, Tennessee 37830, USA

<sup>2</sup>Department of Physics and Astronomy, Brigham Young University, Provo, Utah 84602, USA

<sup>3</sup>Neutron Scattering Division, Oak Ridge National Laboratory, Oak Ridge, Tennessee 37830, USA

<sup>4</sup>Centre for Molecular and Materials Science, TRIUMF, Vancouver, British Columbia, Canada V6T 2A3

<sup>5</sup>Department of Electrical and Computer Engineering, North Carolina State University, Raleigh, North Carolina 27606, USA

<sup>6</sup>Beijing National Laboratory for Condensed Matter Physics, Institute of Physics, Chinese Academy of Sciences, Beijing 100190, People's Republic of China



(Received 22 December 2023; revised 20 May 2024; accepted 6 June 2024; published 24 June 2024)

Manganese telluride (MnTe) is a prospective platform for ultrafast carrier dynamics, spin-based thermoelectrics, and magnon-drag transport due to its unique electronic and magnetic properties. We use inelastic neutron scattering to study both pure and lithium-doped MnTe, focusing on the influence of doping in opening a magnon gap. We use neutron powder diffraction to determine critical exponents for the phase transition in both pure and Li-doped MnTe and complement this information with muon spin rotation/relaxation. The opening of the magnon gap and spin reorientation in Li-doped MnTe is mainly due to increased magnetic anisotropy along the [001] axis, a feature not present in pure MnTe.

DOI: [10.1103/PhysRevB.109.214434](https://doi.org/10.1103/PhysRevB.109.214434)

### I. INTRODUCTION

The interactions between magnons and electrons or phonons creates the physical foundations of modern spintronic applications [1–4]. Recent research in both fundamental and applied spintronics has increasingly emphasized the significance of magnon-mediated interactions, which include magnon spin conductance [5], magnon-drag effects [6,7], magnon-photon interactions [8,9], magnon-phonon interactions [10,11], and magnon-based computing [4,12], among many others. Previous research explored magnon transport properties for various spintronics applications and how a gap affects the transport [13,14]. The magnetic anisotropy of a material often determines the magnon gap energy and provides vital information, such as magnetic ordering, stability, and excitations in magnetic phases [15–17]. The ability to tune the magnetic anisotropy is highly desirable because it enables the manipulation of magnetic structure through spin reorientation [18,19]. In this regard, manganese telluride (MnTe) offers an ideal platform for the investigation of magnon-mediated interactions and transport properties, spin-reorientation phenomena, the interplay between the magnon gap and magnetic anisotropy, and their tunability via chemical doping.

MnTe has been extensively investigated for its magnetic [20–22], thermoelectric [23], electronic [24], and optical properties [25]. It is a magnetic semiconductor (*p* type) with hexagonal NiAs-type structure (space group  $P6_3/mmc$ ) and has a relatively high Néel temperature ( $T_N \approx 307$  K) [20,26],

below which it develops type-A antiferromagnetism, where  $Mn^{2+}$  spins (with  $S = 5/2$ ) exhibit in-plane ferromagnetic ordering along the  $\langle 110 \rangle$  direction, coupled antiferromagnetically along the *c* axis. The magnetic structure and spin waves in MnTe were previously modeled by using a Heisenberg Hamiltonian with isotropic exchange terms up to three nearest neighbors [27]. The magnetic propagation wave vector is (000), and two magnon modes were observed, one ungapped and one gapped [27]. Manganese telluride is also the first antiferromagnet in which a magnon-drag effect was observed [6]. Recently, MnTe was identified as a candidate for *altermagnetism* with collinear antiferromagnetism and broken time-reversal symmetry that could exhibit an anomalous Hall effect [28–30] and was shown to exhibit record piezomagnetism [31]. Consequently, a more in-depth study of the relationship between the properties associated with altermagnetism and the magnons and magnetic structure of MnTe is warranted to elucidate any potential for control or tunability.

In this paper, we use inelastic neutron scattering to study the effects of Li doping on MnTe, which results in the formation of a magnon gap, and we use neutron powder diffraction and muon spin relaxation/rotation ( $\mu$ SR) to estimate the critical exponent of the magnetic phase transition. Subsequently, we explain the tunability of the magnon gap via magnetic anisotropy (single-ion anisotropy) by using complementary linear spin wave theory (LSWT) and density functional theory (DFT) calculations.

### II. EXPERIMENTAL METHODS

Both pure and 5% Li-doped MnTe samples were synthesized following established procedures [7,32,33].

\*Contact author: yumnamg@ornl.gov

†Contact author: hermannrp@ornl.gov

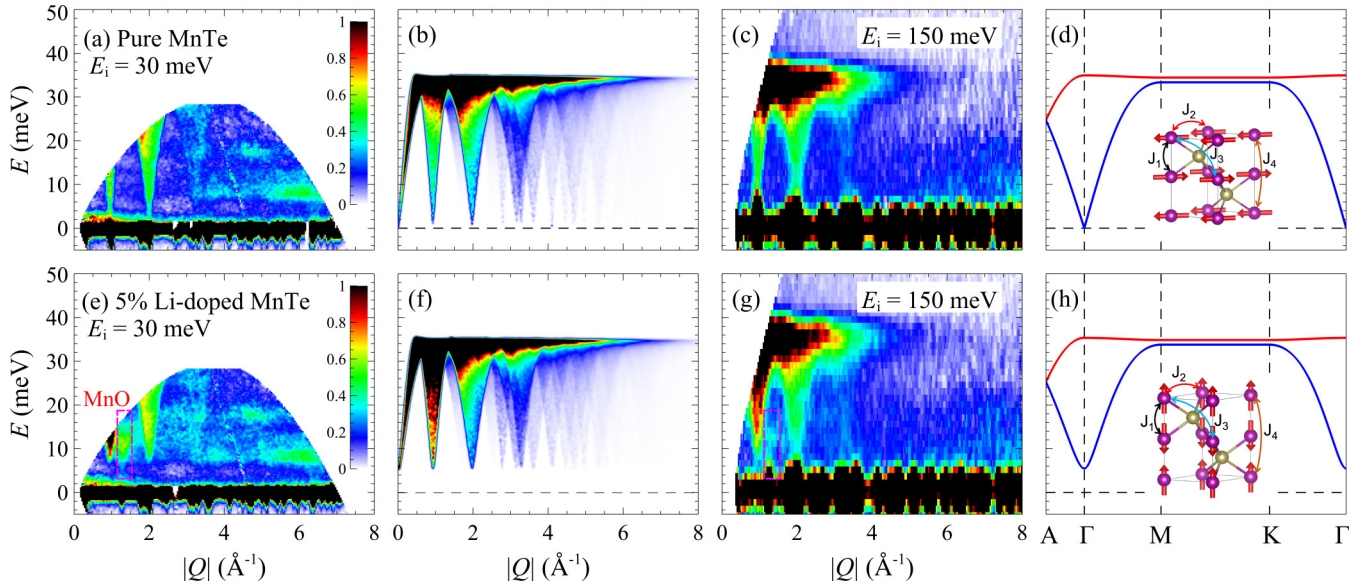


FIG. 1. The powder magnon spectra from inelastic neutron scattering of pure and 5% Li-doped MnTe at  $T = 10$  K as a function of the wave-vector transfer  $|Q|$ , showing experimental data with an incident energy of (a) and (e)  $E_i = 30$  meV and (c) and (g)  $E_i = 150$  meV. Extra magnon intensity attributed to an MnO impurity is observed in Li-doped MnTe [highlighted in (e) and (g) by the dashed magenta rectangle]. The color bar represents the intensity as  $S(Q, E)$  in arbitrary units. (b) and (f) show LSWT simulated powder magnon spectra, and (d) and (h) show calculated momentum-resolved magnon spectra based on the same LSWT model. The insets show the magnetic structures and the exchange interaction terms used in the LSWT calculations.

High-resolution neutron diffraction was performed at the POWDER (HB2A) instrument at the High Flux Isotope Reactor (HFIR) of Oak Ridge National Laboratory. Rietveld refinement using FULLPROF [34] showed that the crystal structures of both pure and doped MnTe have the  $P6_3/mmc$  space group with lattice parameters  $a = 4.121$  Å and  $c = 6.650$  Å for pure MnTe and  $a = 4.108$  Å and  $c = 6.657$  Å for 5% Li-doped MnTe at  $T = 4$  K (See Table S1 in the Supplemental Material [35] for more detail). Analysis of the pure MnTe composition revealed the presence of 3 wt % MnTe<sub>2</sub>, while the Li-doped MnTe sample revealed the presence of 3.1 wt % MnO. We then performed inelastic neutron scattering (INS) on the Wide Angular-Range Chopper Spectrometer (ARCS) [36] at the Spallation Neutron Source (SNS) for powder samples of pure and 5% Li-doped MnTe to investigate the role of Li doping in the magnon dispersion of MnTe. We measured polycrystalline samples because single crystals of Li-doped MnTe were not available. Inelastic neutron scattering serves as an effective tool for probing magnetic excitations because it provides direct access to the spin-spin correlation function,  $S^{m,n}(\mathbf{Q}, E) \propto \sum_{\mathbf{R}\mathbf{R}'} \int e^{iEt/\hbar} e^{-i\mathbf{Q}\cdot(\mathbf{R}-\mathbf{R}')} \langle S_{\mathbf{R}}^m(t) S_{\mathbf{R}'}^n(0) \rangle dt$ , where  $\mathbf{Q}$  is the wave-vector transfer, defined as  $\mathbf{Q} = \mathbf{k}_i - \mathbf{k}_f$ , where  $\mathbf{k}_i$  and  $\mathbf{k}_f$  are the initial and final wave vectors of the scattered neutron, and  $m$  and  $n$  are the spin components. The magnon spectra of the system can be obtained from the inelastic neutron scattering cross section. The magnon dispersion of a material provides critical information about the magnetic structure and dynamics, such as the exchange interaction, magnetic anisotropy, stiffness, and damping. Pure and 5% Li-doped MnTe were measured using INS on ARCS for various incident neutron energies ( $E_i = 30, 60, 75,$  and  $150$  meV) and temperatures ( $T = 10, 20, 40, 60, 80, 100, 175,$  and  $298$  K).

*Density functional theory calculations.* First-principles calculations were performed within the linearized augmented plane-wave approach, using the all-electron density-functional theory code WIEN2K [37]. The experimentally determined crystallographic and magnetic (i.e., alternating Mn magnetic planes) structure was employed, along with a  $U$  value of 5 eV applied to the Mn  $3d$  orbitals. Spin-orbit coupling was applied to determine the magnetic anisotropy, and lithium alloying was modeled via the virtual crystal approximation (VCA), with lithium assumed to substitute in a monovalent manner for divalent Mn. Sufficient numbers of  $k$  points were employed to allow an accurate estimate of magnetic anisotropy. The increase in magnetic anisotropy associated with lithium alloying was reported earlier [32] and mimics the increase in the single-ion magnetic anisotropy term  $K$  assumed in the spin-wave gaps depicted in Fig. 2 below, although the magnitudes observed experimentally are smaller than these calculated values, with the difference potentially due to the frequent overstatement of anisotropy by the VCA.

### III. RESULTS AND DISCUSSION

*Inelastic neutron scattering.* We consider magnon powder spectra with incident energy  $E_i = 30$  meV at  $T = 10$  K for pure and Li-doped MnTe, as shown in Figs. 1(a) and 1(e), respectively. The higher-energy regime is captured in measurements with  $E_i = 150$  meV, as shown in Figs. 1(c) and 1(g), which highlights the upper limits of the magnon spectra around 35 meV, albeit with a lower energy resolution. The energy resolution of the INS measurements at ARCS is given by the full width at half maximum that is 3%–5% of  $E_i$ ; i.e., measurements at  $E_i = 30$  and 150 meV have an

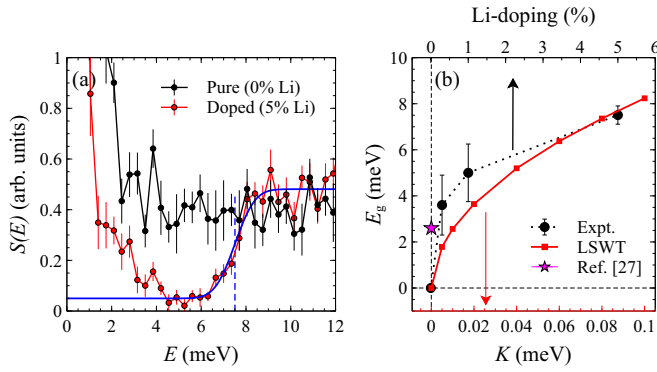


FIG. 2. Magnon gap dependence on the doping concentration of Li. (a)  $S(E)$  integrated over  $Q = 0.929\text{--}0.949 \text{ \AA}^{-1}$  for pure and 5% Li-doped MnTe. (b) Magnon gap with respect to the single-ion anisotropy  $K$  used in LSWT calculations in comparison to the magnon gap with respect to the Li-doping concentration. The pseudogap of  $E_g \simeq 2.6$  meV from Ref. [27] is shown as a star.

energy resolution of 0.9–1.5 and 4.5–7.5 meV, respectively. A previous INS study [27] estimated a 2.6 meV *pseudogap* at the  $\Gamma$  point of pure MnTe, which is an overlap of gapped and ungapped magnons. However, lithium doping transforms the magnon spectra in MnTe, introducing a  $\sim 6$  meV gap, as shown in Figs. 1(e) and 1(g). Note the presence of MnO impurity magnons at  $|Q| \simeq 1.2\text{--}1.5 \text{ \AA}^{-1}$ . The presence of this impurity does not affect our analysis and interpretation of the magnon dispersion. From Figs. 1(c) and 1(g), we observe that both the pure and doped MnTe have the same cutoff in magnon energy, although the cutoff in doped MnTe is more broadened at higher energies, which might indicate some disorder in exchange constants. Unavoidably, there is some low-lying ( $E > 5$  meV) phonon mode scattering at higher  $|Q|$ , visible as bands with intensity proportional to  $Q^2$ .

*Spin wave calculation.* Within a strong correlation limit, the magnon dispersion is described by a Heisenberg spin Hamiltonian of the form

$$H_S = - \sum_{ij} J_{ij} \mathbf{S}_i \cdot \mathbf{S}_j - \sum_i K |S_i^z|^2, \quad (1)$$

where  $J_{ij}$  represents the exchange constant between the  $i$  and  $j$  ions,  $K$  is the single-ion magnetic anisotropy term, and  $\mathbf{S}_i$  is the spin vector of the  $i$ th ion. In our notation, negative (positive) values of  $J_{ij}$  favor antiferromagnetic (ferromagnetic) states. We performed LSWT-based calculations using SPINW [38] to simulate the magnon spectra in the polycrystalline average by using a model with four nearest-neighbor exchange constants  $J_n$  ( $n = 1, 2, 3, 4$ , where  $n$  denotes the  $n$ th-nearest neighbor of a given Mn atom) and a single-ion magnetic anisotropy term  $K$ , as shown in the inset of Fig. 1(d) for pure MnTe and the inset of Fig. 1(h) for doped MnTe. In our model, the spins are oriented along the [110] and [001] directions for pure and doped MnTe, respectively. Spins are antiferromagnetically coupled along the  $c$  axis, which is in agreement with Rietveld refinements and representational analysis [32,33]. Furthermore, the single-ion anisotropy term was set to zero ( $K = 0$ ) in pure MnTe, whereas in the Li-doped MnTe we set

$K = 0.08$  meV, a value of  $K$  determined by comparing the LSWT simulated powder spectra with experimental magnon spectra; see spectra simulated on the basis of this model in Figs. 1(b) and 1(f) for pure and doped MnTe, respectively. For both pure and Li-doped MnTe, we used exchange constants  $J_n$  (as defined above) obtained from DFT-based simulations [39], which are given as  $J_1 = -4.125$  meV,  $J_2 = -0.025$  meV,  $J_3 = -0.55$  meV, and  $J_4 = -0.2175$  meV, noting a factor of  $S^2$  ( $S = 5/2$ ) difference in the normalization. The symmetry-allowed exchange matrix is given by the symmetry of the crystal structure and it has a magnetic wave vector  $\mathbf{k} = 0$ . This is equally true for the system with Li doping. The simulated magnon spectra from our LSWT model based on the exchange constants given above agree very well within the experimental resolution with our INS powder-averaged magnon spectra, as shown in Figs. 1(a)–1(c) and 1(e)–1(g).

*Magnon gap tunability.* The magnon gap  $E_g$  in Li-doped MnTe is directly related to single-ion magnetic anisotropy, where  $E_g \sim K(S^z)$ . Simulated LSWT momentum-resolved magnon spectra are shown in Fig. 1(d) for pure MnTe and Fig. 1(h) for 5% Li-doped MnTe. In pure MnTe, we see a gapped magnon mode and an ungapped magnon mode, which agrees well with a previous report [27]. In contrast, in the doped MnTe we see two magnon modes, both gapped at the  $\Gamma$  point. A closer comparison of the two magnon modes in pure and doped MnTe reveals that the ungapped mode in pure MnTe (shown in blue) transforms into a gapped magnon upon Li doping (also shown in blue). The gapped magnon mode in pure MnTe (shown in red) is visually unchanged upon Li doping (also shown in red). To quantify the gap, we integrated  $S(E)$  in the  $Q = 0.929\text{--}0.949 \text{ \AA}^{-1}$  range for pure and 5% Li-doped MnTe [see Fig. 2(a)]. For the estimation of the magnon gap in pure MnTe (0% Li) and 5% Li-doped MnTe, we chose the INS measurements at  $T = 10$  K and  $E_i = 30$  meV. Due to the unavailability of 10 K and 30 meV data for 0.3% and 1% Li-doped MnTe, we chose the INS measurements at  $T = 150$  K and  $E_i = 60$  meV, which are the lowest available  $T$  and  $E_i$ . See the Appendix for a description of how the magnon gap cuts were obtained, as demonstrated for 0.3% and 1% Li-doped MnTe in Figs. 5 and 6. In the  $T = 150$  K and  $E_i = 60$  meV data for 0.3% and 1% Li-doped MnTe, some magnetic low-energy quasielastic scattering was also observed which was absent at  $T = 10$  K. For the 150 K data, we subtracted this quasielastic scattering before estimating the *incipient* magnon gap, as described in the Appendix. We estimate the magnon gap  $E_g$ , shown in Fig. 2(b) by black circles, by fitting to an error function of the form  $A \text{erf}(x - E_g) + B$ , where  $A$  and  $B$  represent a fitted scale factor and a fitted offset for the error function, respectively. The  $\text{erf}(x)$  function is the primitive of the normal distribution. The magnon gap energy as a function of the single-ion anisotropy term  $K$  is obtained from the LSWT-based magnon spectra with the magnetic structure configuration of the Li-doped MnTe, as shown in Fig. 2(b) by red squares (see the Appendix, Figs. 7 and 8). We note that Fig. 2(b) assumes a linearity in the dependence of  $E_g$  with respect to  $K$  and the Li-doping concentration. Figure 2 demonstrates the tunability of the magnon gap energy or magnon dispersion as a function of magnetic anisotropy  $K$ . The controllability of the magnon dispersion by tuning the magnetic anisotropy suggests the possibility

to design switchable devices with contrasting magnon group velocity, which is defined as  $v_g^m = (\delta E / \delta q) = \hbar(\delta \omega / \delta q)_{q \rightarrow \Gamma}$ .  $v_g^m$  is dependent on the slope of the magnon dispersion near the  $\Gamma$  point, which is significantly different for pure and Li-doped MnTe [see Figs. 1(d) and 1(h)]. Generally, magnetic anisotropy is sensitive to the electronic structure near the Fermi level, which is easily perturbed via external parameters such as temperature, pressure, and chemical doping and associated structural changes. Examples of these include the planar-to-uniaxial transition with increasing temperature in  $\text{Nd}_2\text{Fe}_{14}\text{B}$  [40], the transition from planar to uniaxial behavior caused by interstitial nitrogen substitution into  $\text{Sm}_2\text{Fe}_{17}$  [41], and the temperature-related magnetostructural transition [42,43] in MnBi associated with a transition from planar to uniaxial behavior. In all these materials, the addition of an external parameter perturbs the near- $E_F$  electronic structure sufficiently to greatly alter the anisotropy of the system. This electronic structure generally derives from the transition metal 3d orbitals, whose exchange constant distance dependence and associated electronic structure alterations originate from magnetoelastic coupling [44]. In view of the large effective spin of Mn ( $S = 5/2$ ), we likewise contend that the change in magnetic anisotropy upon Li doping is due to a combination of this aforementioned coupling and the charge alloying due to lithium substitution.

The presence of a magnon gap of  $\sim 6$  meV (70 K) for the Li-doped sample but not the pure MnTe sample is expected to lead to disparate low-temperature magnon-associated transport behaviors in both the spin and magnon-associated heat transport channels, stemming from the Bose-Einstein distribution applicable to bosonic magnon excitations. In particular, below approximately 50 K, we expect that, in the Li-alloyed material, these transport channels will experience an exponential suppression [i.e., the thermal factor  $(e^{\hbar\omega_G/k_B T} - 1)^{-1}$ ], whereas the ungapped pure sample should experience a power-law (in temperature) behavior. It is anticipated that magnetic scattering, as well as the evident compositional disorder in the alloyed sample, will significantly impact the quantitative interpretation of these results; see Ref. [45] for an example of such an interpretation.

**Order parameter.** The (001) magnetic reflection at  $Q = 0.939 \text{ \AA}^{-1}$  in pure MnTe disappears completely in Li-doped MnTe due to the reorientation of the spins along the  $c$  axis upon Li doping [32]. To determine the behavior of both pure and Li-doped MnTe near the phase transition, we analyze the neutron powder diffraction data previously published in Ref. [32] in more detail. Figure 3(a) shows the Rietveld refinement of HB-2A neutron powder diffraction data of pure MnTe at 4 K. Similarly, Fig. 3(c) shows the Rietveld refinement of neutron powder diffraction of 5% Li-doped MnTe at 4 K. Note the presence of MnO impurity peaks highlighted in the shaded boxes, which are excluded in our refinement. A detailed investigation determining the Li site using Rietveld refinement indicated that Li most likely occupies the Wyckoff 2d sites in comparison to other sites like 2a and 2c, which is consistent with Ref. [32]. The next best fit was provided by Li occupying 2a sites (i.e., Mn sites), which is consistent with the defect analysis based on transport measurements presented in Ref. [7] that indicated Li ions can be present as a neutral state (effective negative charge) in the interstitial (Mn) site, i.e.,

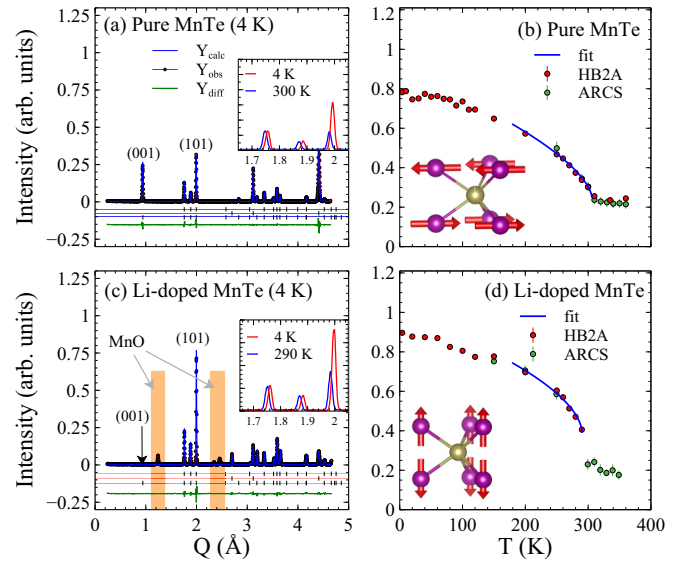


FIG. 3. Neutron powder diffraction data from HB-2A (from Ref. [32]) showing magnetic peaks (001) and (101) and highlighting the difference between (a) pure MnTe and (c) Li-doped MnTe. Rietveld refinement was used to resolve the crystal and magnetic structure. The observed (red), refined (blue), and data-fit (green) curves are labeled. Magnetic MnO impurity reflections, which are excluded in our fit are highlighted by the shaded boxes in (c). The insets of (a) and (c) show the observed reflections between  $Q = 1.65$  and  $2.05 \text{ \AA}^{-1}$  at  $T = 4 \text{ K}$  and  $T > T_N$ . The peaks from the structure (green), aluminum sample container (red), and magnetic component (blue) used in our refinement are also shown. (b) and (d) show the order parameter (OP) from the (101) reflection of (b) pure MnTe and (d) Li-doped MnTe from the ARCS (green circles) and HB-2A (red circles) instruments. Note that the (101) reflection contains nuclear and magnetic contributions and so does not vanish above  $T_N$ . The OP is fitted by a power-law expression, as shown by blue lines. The insets in (b) and (d) illustrate the magnetic spin orientation. Error bars represent one standard deviation. The magnetic structure analysis of the HB-2A diffraction data was reported in Ref. [32] and is analyzed here in the critical regime together with ARCS diffraction data.

the 2d (2a) site. We analyzed the magnetic ordering in both pure and Li-doped MnTe by focusing on the (101) peak at  $Q \sim 2 \text{ \AA}^{-1}$ , noting the absence of the (001) peak in Li-doped MnTe [see Figs. S1 and S2 in the Supplemental Material for the estimation of the order parameter from Gaussian fitting of the (101) reflection]. The (101) peak comprises the (101) magnetic reflection superimposed onto the (101) structural reflection. We also used elastic cut diffraction data of the neutron inelastic scattering performed at ARCS to supplement the data for magnetic ordering at higher temperature. The elastic cuts were performed by using an energy integration from  $E_i = -1$  to  $+1$  meV.

The magnetic order parameter is derived from a Gaussian fitting of the (101) reflection and fitted with a power-law expression given as  $A(1 - T/T_N)^{2\beta}$ , where  $T_N$  is the Néel temperature,  $\beta$  is the critical exponent, and  $A$  is the intensity scaling constant. The fitted parameters are presented in Table I, which shows that Li doping induces a small reduction of both  $\beta$  and  $T_N$ . A closer look at the temperature dependence

TABLE I. The magnetic order parameters fitted by using a power-law relation in pure and doped MnTe via neutron powder diffraction (NPD) and muon spin rotation ( $\mu$ SR).  $\mu$ SR probes the local or intermediate range (IR) correlation. We also include critical exponents from the magnetic pair distribution function (mPDF) based total scattering analysis which probes both long-range (LR) and short-range (SR) correlations from Ref. [46] for completeness.

MnTe	Method	$\beta$	$T_N$ (K)
Pure	NPD	0.317(20)	305.9 (2.0)
	mPDF (LR)	0.300(30)	304.5 (3.0)
	$\mu$ SR (IR)	0.450(10)	307.5 (0.1)
	mPDF (SR)	0.710(50)	302.0 (3.0)
Doped	NPD	0.285(30)	290.3 (1.0)

of this (001) reflection of Li-doped MnTe as measured at ARCS revealed a transient temperature range (290–350 K), where a significant order-parameter spin correlation persists, which indicates a temperature-dependent weak fluctuation of the spins perpendicular to the [001] direction near  $T_N$  [46] (see the inset in Fig. S2 in the Supplemental Material [35]).

Table I shows a monotonic progression of  $\beta$  from  $\sim 0.3$  for long-range correlations probed by neutron powder diffraction (NPD) or long-range (LR) magnetic pair distribution function (mPDF) to  $\sim 0.45$  for intermediate-range correlations probed by  $\mu$ SR and  $\sim 0.71$  for the shortest-range (SR) correlations probed by mPDF, i.e., nearest-neighbor magnetic correlations. mPDF can probe magnetic correlations on various length scales based on the range of real-space mPDF data used for the analysis. If we look just at the nearest-neighbor magnetic correlations in MnTe using mPDF, i.e., SR mPDF, and compare them to the long-range correlations, i.e., LR mPDF, we see an obvious difference in the development of magnetic correlation with respect to temperature [46]. Unlike the pure MnTe, the NPD-derived  $\beta$  of Li-doped MnTe clearly deviates from a conventional three-dimensional Ising antiferromagnet ( $\beta = 0.326$ ) [47]. The decreasing of Néel temperature  $T_N$  in doped MnTe indicates a lowered exchange-coupling strength compared to the pure MnTe. In order to investigate the change in the exchange constants due to Li doping, we performed DFT calculations based on a simple model consisting of only two exchange constants ( $J'_1$  and  $J'_2$ ). As shown in Table II, the exchange constants of the Li-doped MnTe are lower than those of pure MnTe, which agrees with the reduction in Néel temperature in experiments. Note that  $J'_1$  and  $J'_2$  obtained here are different from the exchange constants  $J_1$ ,  $J_2$ ,  $J_3$ , and  $J_4$  used in our LSWT model, which were obtained from DFT calculations for pure MnTe.

TABLE II. The exchange constants ( $J'_1$  and  $J'_2$ ) obtained from density functional theory calculations. Virtual crystal approximation was used to model the Li doping.

MnTe	$J'_1$ (meV)	$J'_2$ (meV)
Pure	-3.36	-0.016
Doped	-3.04	-0.008

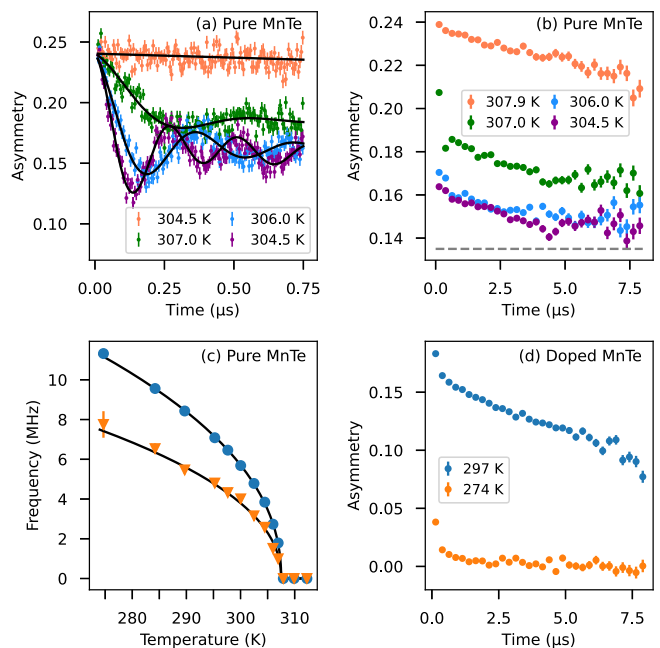


FIG. 4. (a) Early-time, zero-field asymmetry spectra of MnTe showing the development of coherent oscillations as long-range magnetic order is established. Black curves are fits to the data using two exponentially damped cosine functions and a slowly decaying tail. (b) Long-time, zero-field asymmetry spectra showing a rapid transition between the paramagnetic state at 307.9 K and the antiferromagnetic (AFM) state with 100% ordered volume fraction at 306 K. The dashed horizontal line represents the constant background asymmetry of 0.135 contributed by the sample holder. (c) Asymmetry oscillation frequency as a function of temperature, which is proportional to the AFM ordered moment. The black curves represent a power-law fit. (d) Long-time, zero-field asymmetry spectra for Li-doped MnTe, showing predominantly paramagnetic behavior at 297 K and a full magnetic volume fraction at 274 K.

*Muon spin-relaxation analysis.* The neutron diffraction-derived analysis of the order-parameter is corroborated by  $\mu$ SR data [48] collected for pure and 5% Li-doped MnTe at TRIUMF. Key results are summarized in Fig. 4. The  $\mu$ SR asymmetry spectra collected from pure MnTe in zero field show coherent oscillations below  $T_N$  with two distinct frequencies [see Fig. 4(a)], reflecting the long-range magnetic order. We performed fits to the spectra to extract the oscillation frequencies as a function of temperature [black curves in Fig. 4(a)]. The relative weight of the two oscillating components was refined as a global parameter in the fit, but the two frequencies were allowed to vary independently. The frequencies extracted from the fits serve as an order parameter for the magnetic transition and are shown in Fig. 4(c). A power-law fit performed for the two sets of frequencies simultaneously [black curves in Fig. 4(c)] yielded  $T_N = 307.5(1)$  K and  $\beta = 0.45(1)$ , which is sizably larger than  $\beta$  determined from the neutron measurements, as shown in Table I. We attribute this to the sensitivity of  $\mu$ SR to local magnetic correlations, in contrast to the long-range correlations probed by neutrons. We also show critical exponents obtained from mPDF analysis

which confirm the trend of higher critical exponents for short-range correlations in Table I [46].

The long-time asymmetry spectra for pure MnTe in Fig. 4(b) show a sharp drop in the long-time tail between 307.9 and 306.0 K, confirming that the full sample volume becomes magnetically ordered in this narrow temperature window. In contrast, the Li-doped sample [Fig. 4(d)] still shows a large paramagnetic fraction at 297 K, confirming the reduction of  $T_N$  with Li doping. No oscillations are observed in the early-time spectra of the doped sample, which is not surprising considering the increased disorder associated with the dopant ions. As a result,  $T_N$  and the critical exponent for the doped sample could not be determined. Comparing Figs. 4(b) and 4(d), the Li-doped MnTe long-time asymmetry goes from  $\sim 0.15$  to 0 near the transition, while the long-time asymmetry of the pure MnTe sample goes from  $\sim 0.24$  to  $\sim 0.15$ . The reason for this difference is that the asymmetry spectra for the pure compound include a constant background of  $\sim 0.135$  arising from the sample holder, while the doped sample was measured in a different sample holder that contributed a negligible background.

#### IV. CONCLUSIONS

Our study sheds light on the effects of Li doping on the magnetic and magnonic properties of MnTe. Pure MnTe undergoes a transition from an easy-plane to an easy-axis antiferromagnet upon Li doping. Inelastic neutron scattering experiments revealed the emergence of an enhanced magnetic anisotropy due to Li doping, resulting in the opening of a magnon gap. This magnon gap in Li-doped MnTe is attributed to the increased magnetic anisotropy along the  $c$  axis, a phenomenon absent in pure MnTe. Muon spin rotation/relaxation data confirmed the transition to a long-range antiferromagnetic state at the Néel temperature ( $T_N = 307$  K) in pure MnTe. Furthermore, linear spin wave theory and inelastic neutron scattering experiments illustrated the alterations in the magnetic structure and magnon dispersion caused by Li doping. Notably, the spin reorientation and magnon gap opening observed in Li-doped MnTe have significant implications for understanding spin-based phenomena and spintronic applications, such as the tunability of the magnon gap via doping or by tuning the magnetic anisotropy of the material. These findings provide valuable insights into the potential use of Li-doped MnTe for advanced magnonic and spintronic device applications.

DOE will provide public access to the results of federally sponsored research in accordance with the DOE Public Access Plan [49]. The neutron scattering data associated with this work is available at Ref. [50].

#### ACKNOWLEDGMENTS

This work was supported by the U.S. Department of Energy (DOE), Office of Science, Basic Energy Sciences, Materials Sciences and Engineering Division. Portions of this research used resources at the Spallation Neutron Source and High Flux Isotope Reactor, which is a U.S. DOE Office of Science User Facility operated by the Oak Ridge

National Laboratory. We acknowledge the assistance of D. L. Abernathy, K. M. Taddei, and S. Calder for neutron data acquisition. Work by B.A.F., C.Z.S., and E.Z. was supported by the U.S. Department of Energy, Office of Science, Basic Energy Sciences (DOE-BES), through Award No. DE-SC0021134. We acknowledge the use of the muon facility at TRIUMF Lab and thank the TRIUMF staff for their assistance with the experiments. M.M.H.P. and D.V. acknowledge the financial support provided by the Air Force Office of Scientific Research (AFOSR) under Contract No. FA9550-23-1-0302, and the National Science Foundation (NSF) under Grant No. CBET-2110603. ORNL is managed by UT-Battelle, LLC, under Contract No. DE-AC05-00OR22725 for the U.S. Department of Energy (DOE). The U.S. government retains and the publisher, by accepting the article for publication, acknowledges that the U.S. government retains a nonexclusive, paid-up, irrevocable, worldwide license to publish or reproduce the published form of this manuscript, or allow others to do so, for U.S. government purposes.

#### APPENDIX: MAGNON GAP DETERMINATION

The magnon gap in 0.3% and 1% Li-doped MnTe is obtained by fitting the  $Q$ -integrated  $S(E)$  around  $Q = 0.929\text{--}0.949\text{\AA}^{-1}$ . We also visually compare these cuts and fits with a similar  $Q$ -integrated  $S(E)$  from the linear spin wave theory calculated powder-averaged magnon dispersion. The estimated magnon gaps from the 0.3%, 1%, and 5% concentrations of Li doping are 3.6 (1.3), 5.0 (1.3), and 7.5 (0.4) meV, respectively. In Fig. 5, we show the process of obtaining the magnon gaps in the case of 0.3% and 1% Li-doped MnTe. As shown in Figs. 5(a) and 5(b), we start by taking the cuts around  $Q_1 = 0.939$ ,  $Q_2 = 1.25$ , and  $Q_3 = 1.45\text{\AA}^{-1}$ , with an integration width of  $dQ = 0.02\text{\AA}^{-1}$ . INS spectra of 0.3% and 1% Li-doped MnTe were measured on ARCS with  $E_i = 60$  meV and  $T = 150$  K (which are the lowest  $E_i$  and  $T$  available for these doping concentrations). The obtained cuts  $S(E)$  are shown in Figs. 5(c) and 5(d). We subtract the magnetic quasielastic scattering by taking the difference in  $S(E)$  from  $Q_1 - Q_2$  and  $Q_1 - Q_3$ . The subtraction of the magnetic quasielastic scattering is performed for two different  $Q$  cases to ensure the correct procedure is applied and check for oversubtraction, as shown in Figs. 5(e) and 5(f).

These background-subtracted cuts were fitted with the error function  $A\text{erf}(x - E_g) + B$ , where  $\text{erf}(x)$  is the error function and  $A$  and  $B$  have the same definition as before. We refer to the magnon gaps obtained in these two cases (0.3% and 1% Li-doped MnTe measured at  $E_i = 60$  meV and  $T = 150$  K) as *incipient* magnon gaps since we performed the subtraction of the magnetic quasielastic scattering. Note that the magnon gap cuts for pure and 5% Li-doped MnTe shown in Fig. 2(a) do not involve the subtraction of the magnetic quasielastic background because they were measured at near-ideal low background conditions ( $E_i = 30$  meV and  $T = 10$  K). As shown in Figs. 2 and 6(b), the magnon gap of 5% Li-doped MnTe is estimated by taking the cuts  $S(E)$  at  $Q_1 = 0.939\text{\AA}^{-1}$ , without performing any further background subtraction. Therefore, we make the clear distinction that the magnon gap estimated in the case of the 5% Li-doped MnTe is not an incipient gap. The fit was

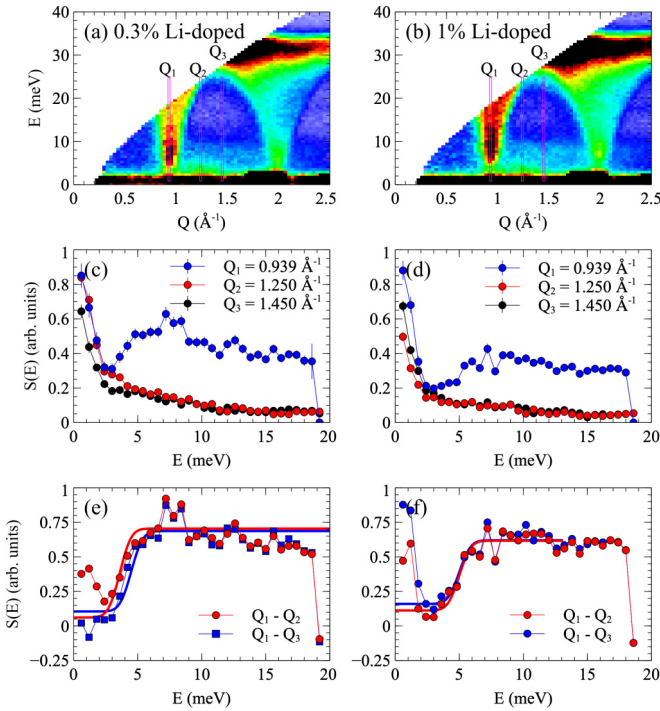


FIG. 5. Magnon gap obtained from fits of  $S(E)$  as shown in the main text. The powder magnon spectra  $S(Q, E)$  of (a) 0.3% and (b) 1% Li-doped MnTe. The  $Q$ -integrated cuts  $S(E)$  with an integration range of  $dQ = 0.02 \text{ \AA}^{-1}$  at  $Q_1 = 0.939$ ,  $Q_2 = 1.25$ , and  $Q_3 = 1.45 \text{ \AA}^{-1}$  are shown for (c) 0.3% and (d) 1% Li-doped MnTe. The magnetic quasielastic scattering subtracted cuts ( $Q_1 - Q_2$  and  $Q_1 - Q_3$ ) and the fits based on an error function,  $\text{Aerf}(x - E_g) + B$ , for (e) 0.3% and (f) 1% Li-doped MnTe.

performed by taking the same function as mentioned above. We note the presence of nonzero intensity at low  $E$ , which is attributed to a limitation of the low-angle detector in the ARCS instrument. The MnO magnons are also avoided in this estimation.

The magnon gaps estimated from the powder-averaged magnon spectra based on the linear spin wave theory (LSWT)

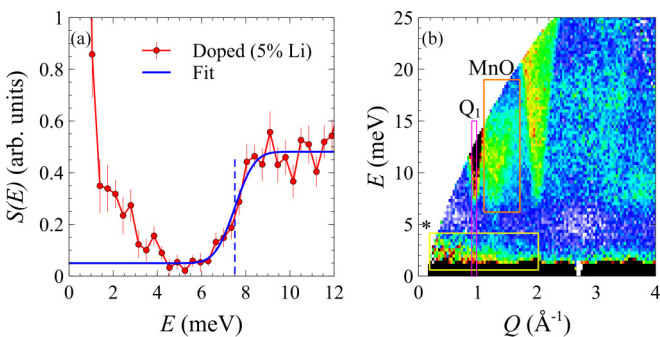


FIG. 6. (a) Magnon gap estimation in the case of 5% Li-doped MnTe is performed by taking  $S(E)$  cuts at  $Q_1$ , shown by the magenta rectangle in (b). The nonzero intensity in  $S(E)$  at low  $E$  (highlighted by the yellow rectangle, near the elastic line) is due to a low-angle detector limitation in the ARCS instrument. The MnO magnons are also highlighted in the orange rectangle.

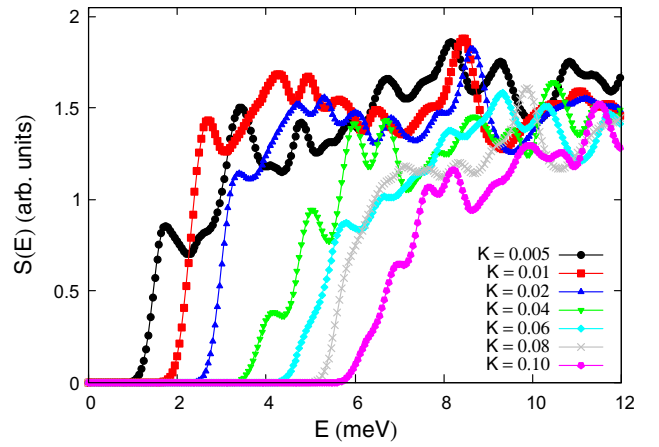


FIG. 7. Magnon gaps from the LSWT calculated powder-averaged magnon spectra using the magnetic structure of the Li-doped MnTe at varying single-ion anisotropy  $K$ .

calculations for different magnetic single-ion anisotropy terms  $K$  are also given in Fig. 7. The integrated  $S(E)$  cuts from the LSWT calculated powder-averaged magnons have squiggles because of the nonuniformity in the averaging method implemented, which does not affect our discussion of the estimated magnon gap. The model used for these calculations is described in detail in the main text. We used the magnetic structure model for the Li-doped MnTe with varying magnetic single-ion anisotropy terms  $K$ . Figure 8 shows the LSWT calculated powder-averaged magnon spectra for different single-ion anisotropies  $K$  as identified in the legend of each panel. Note that the powder average magnon dispersion is calculated by considering the instrument resolution as described in the main text; i.e., the ARCS instrument has an energy resolution of 3%–5% of  $E_i$ , and therefore, we take 0.9 meV as our energy resolution in the LSWT calculations.

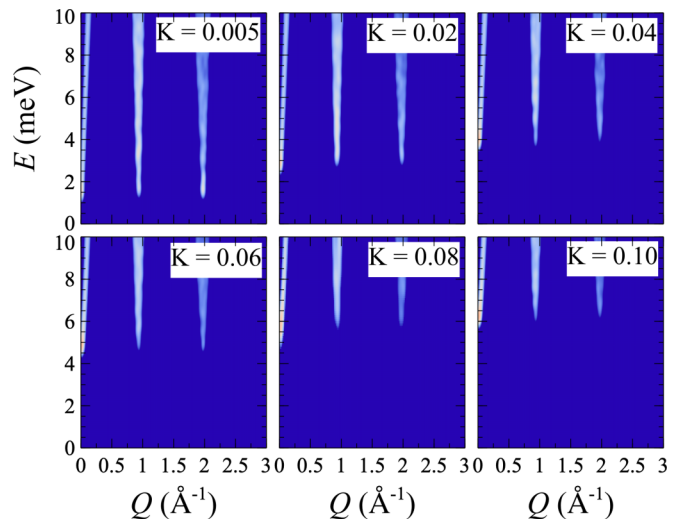


FIG. 8. Magnon gaps from linear spin wave theory calculations were estimated as a function of single-ion anisotropy  $E_g(K)$ .

- [1] A. A. Serga, A. V. Chumak, and B. Hillebrands, YIG magnonics, *J. Phys. D* **43**, 264002 (2010).
- [2] B. Lenk, H. Ulrichs, F. Garbs, and M. Münzenberg, The building blocks of magnonics, *Phys. Rep.* **507**, 107 (2011).
- [3] A. V. Chumak, A. A. Serga, and B. Hillebrands, Magnon transistor for all-magnon data processing, *Nat. Commun.* **5**, 4700 (2014).
- [4] H. Yuan, Y. Cao, A. Kamra, R. A. Duine, and P. Yan, Quantum magnonics: When magnon spintronics meets quantum information science, *Phys. Rep.* **965**, 1 (2022).
- [5] L. J. Cornelissen, J. Liu, B. J. van Wees, and R. A. Duine, Spin-current-controlled modulation of the magnon spin conductance in a three-terminal magnon transistor, *Phys. Rev. Lett.* **120**, 097702 (2018).
- [6] G. Zanmarchi and C. Haas, Magnon drag, *Philips Res. Rep.* **23**, 389 (1968).
- [7] M. M. H. Polash, D. Moseley, J. Zhang, R. P. Hermann, and D. Vashaee, Understanding and design of spin-driven thermoelectrics, *Cell Rep. Phys. Sci.* **2**, 100614 (2021).
- [8] L. Bai, M. Harder, Y. P. Chen, X. Fan, J. Q. Xiao, and C.-M. Hu, Spin pumping in electrodynamically coupled magnon-photon systems, *Phys. Rev. Lett.* **114**, 227201 (2015).
- [9] H. Y. Yuan and X. R. Wang, Magnon-photon coupling in antiferromagnets, *Appl. Phys. Lett.* **110**, 082403 (2017).
- [10] T. Hioki, Y. Hashimoto, and E. Saitoh, Coherent oscillation between phonons and magnons, *Commun. Phys.* **5**, 115 (2022).
- [11] C. Berk, M. Jaris, W. Yang, S. Dhuey, S. Cabrini, and H. Schmidt, Strongly coupled magnon-phonon dynamics in a single nanomagnet, *Nat. Commun.* **10**, 2652 (2019).
- [12] F. Heussner, M. Nabinger, T. Fischer, T. Brächer, A. A. Serga, B. Hillebrands, and P. Pirro, Frequency-division multiplexing in magnonic logic networks based on caustic-like spin-wave beams, *Phys. Status Solidi RRL* **12**, 1800409 (2018).
- [13] D. D. Vu, R. A. Nelson, B. L. Wooten, J. Barker, J. E. Goldberger, and J. P. Heremans, Magnon gap mediated lattice thermal conductivity in  $\text{MnBi}_2\text{Te}_4$ , *Phys. Rev. B* **108**, 144402 (2023).
- [14] J. Aftergood and S. Takei, Conductivity enhancement in a diffusive Fermi liquid due to Bose-Einstein condensation of magnons, *Phys. Rev. Lett.* **130**, 086702 (2023).
- [15] N. Ntallis, V. Borisov, Y. O. Kvashnin, D. Thonig, E. Sjöqvist, A. Bergman, A. Delin, O. Eriksson, and M. Pereiro, Connection between magnetic interactions and the spin-wave gap of the insulating phase of  $\text{NaOsO}_3$ , *Phys. Rev. B* **104**, 134433 (2021).
- [16] M. G. Pini, P. Politi, and R. L. Stamps, Anisotropy effects on the magnetic excitations of a ferromagnetic monolayer below and above the Curie temperature, *Phys. Rev. B* **72**, 014454 (2005).
- [17] W. Rudziński, Effect of single-ion anisotropy on magnons in the  $\text{VSe}_2$  bilayer antiferromagnet, *J. Magn. Magn. Mater.* **546**, 168687 (2022).
- [18] L. J. Cornelissen, J. Liu, R. A. Duine, J. B. Youssef, and B. J. van Wees, Long-distance transport of magnon spin information in a magnetic insulator at room temperature, *Nat. Phys.* **11**, 1022 (2015).
- [19] B. Mali, J. Sunil, H. S. Nair, C. Narayana, and S. Elizabeth, Spin reorientation to a  $\Gamma_3(C_x, F_y, A_z)$  configuration and anisotropic spin-phonon coupling in a  $\text{Sm}_{0.5}\text{Y}_{0.5}\text{FeO}_3$  single crystal, *Phys. Rev. B* **105**, 214417 (2022).
- [20] T. Komatsubara, M. Murakami, and E. Hirahara, Magnetic properties of manganese telluride single crystals, *J. Phys. Soc. Jpn.* **18**, 356 (1963).
- [21] J. Wasscher, Evidence of weak ferromagnetism in  $\text{MnTe}$  from galvanomagnetic measurements, *Solid State Commun.* **3**, 169 (1965).
- [22] C. F. Squire, Antiferromagnetism in some manganese compounds, *Phys. Rev.* **56**, 922 (1939).
- [23] J. Wasscher and C. Haas, Contribution of magnon-drag to the thermoelectric power of antiferromagnetic  $\text{MnTe}$ , *Phys. Lett.* **8**, 302 (1964).
- [24] M. Podgorny and J. Oleszkiewicz, Electronic structure of antiferromagnetic  $\text{MnTe}$ , *J. Phys. C* **16**, 2547 (1983).
- [25] G. Zanmarchi, Optical measurements on the antiferromagnetic semiconductor  $\text{MnTe}$ , *J. Phys. Chem. Solids* **28**, 2123 (1967).
- [26] D. Kriegner, H. Reichlova, J. Grenzer, W. Schmidt, E. Ressouche, J. Godinho, T. Wagner, S. Y. Martin, A. B. Shick, V. V. Volobuev, G. Springholz, V. Holý, J. Wunderlich, T. Jungwirth, and K. Výborný, Magnetic anisotropy in antiferromagnetic hexagonal  $\text{MnTe}$ , *Phys. Rev. B* **96**, 214418 (2017).
- [27] W. Szuskiewicz, E. Dynowska, B. Witkowska, and B. Hennion, Spin-wave measurements on hexagonal  $\text{MnTe}$  of NiAs-type structure by inelastic neutron scattering, *Phys. Rev. B* **73**, 104403 (2006).
- [28] R. D. Gonzalez Betancourt, J. Zubáč, R. Gonzalez-Hernandez, K. Geishendorf, Z. Šobán, G. Springholz, K. Olejník, L. Šmejkal, J. Sinova, T. Jungwirth, S. T. B. Goennenwein, A. Thomas, H. Reichlová, J. Železný, and D. Kriegner, Spontaneous anomalous Hall effect arising from an unconventional compensated magnetic phase in a semiconductor, *Phys. Rev. Lett.* **130**, 036702 (2023).
- [29] L. Šmejkal, J. Sinova, and T. Jungwirth, Emerging research landscape of altermagnetism, *Phys. Rev. X* **12**, 040501 (2022).
- [30] I. I. Mazin, Altermagnetism in  $\text{MnTe}$ : Origin, predicted manifestations, and routes to detwinning, *Phys. Rev. B* **107**, L100418 (2023).
- [31] R. Baral, A. M. Abeykoon, B. J. Campbell, and B. A. Frandsen, Giant spontaneous magnetostriction in  $\text{MnTe}$  driven by a novel magnetostructural coupling mechanism, *Adv. Funct. Mater.* **33**, 2305247 (2023).
- [32] D. H. Moseley, K. M. Taddei, J. Yan, M. A. McGuire, S. Calder, M. M. H. Polash, D. Vashaee, X. Zhang, H. Zhao, D. S. Parker, R. S. Fishman, and R. P. Hermann, Giant doping response of magnetic anisotropy in  $\text{MnTe}$ , *Phys. Rev. Mater.* **6**, 014404 (2022).
- [33] Y. Zheng, T. Lu, M. M. H. Polash, M. Rasoulianboroujeni, N. Liu, M. E. Manley, Y. Deng, P. J. Sun, X. L. Chen, R. P. Hermann, D. Vashaee, J. P. Heremans, and H. Zhao, Paramagnon drag in high thermoelectric figure of merit Li-doped  $\text{MnTe}$ , *Sci. Adv.* **5**, eaat9461 (2019).
- [34] J. Rodríguez-Carvajal, Recent advances in magnetic structure determination by neutron powder diffraction, *Phys. B (Amsterdam, Neth.)* **192**, 55 (1993).
- [35] See Supplemental Material at <http://link.aps.org/supplemental/10.1103/PhysRevB.109.214434> for Rietveld refinement of neutron powder diffraction and estimation of order parameters from (101) reflections.

- [36] D. L. Abernathy, M. B. Stone, M. J. Loguillo, M. S. Lucas, O. Delaire, X. Tang, J. Y. Y. Lin, and B. Fultz, Design and operation of the wide angular-range chopper spectrometer ARCS at the Spallation Neutron Source, *Rev. Sci. Instrum.* **83**, 015114 (2012).
- [37] P. Blaha, K. Schwarz, F. Tran, R. Laskowski, G. K. H. Madsen, and L. D. Marks, WIEN2k: An APW+lo program for calculating the properties of solids, *J. Chem. Phys.* **152**, 074101 (2020).
- [38] S. Toth and B. Lake, Linear spin wave theory for single-q incommensurate magnetic structures, *J. Phys.: Condens. Matter* **27**, 166002 (2015).
- [39] S. Mu, R. P. Hermann, S. Gorsse, H. Zhao, M. E. Manley, R. S. Fishman, and L. Lindsay, Phonons, magnons, and lattice thermal transport in antiferromagnetic semiconductor MnTe, *Phys. Rev. Mater.* **3**, 025403 (2019).
- [40] M. A. Susner, B. S. Conner, B. I. Saporov, M. A. McGuire, E. J. Crumlin, G. M. Veith, H. Cao, K. V. Shanavas, D. S. Parker, B. C. Chakoumakos, and B. C. Sales, 2Flux growth and characterization of Ce-substituted Nd<sub>2</sub>Fe<sub>14</sub>B single crystals, *J. Magn. Magn. Mater.* **434**, 1 (2017).
- [41] T. Pandey, M.-H. Du, and D. S. Parker, Tuning the magnetic properties and structural stabilities of the 2-17-3 magnets Sm<sub>2</sub>Fe<sub>17</sub>X<sub>3</sub> (X = C, N) by substituting La or Ce for Sm, *Phys. Rev. Appl.* **9**, 034002 (2018).
- [42] M. A. McGuire, H. Cao, B. C. Chakoumakos, and B. C. Sales, Symmetry-lowering lattice distortion at the spin reorientation in MnBi single crystals, *Phys. Rev. B* **90**, 174425 (2014).
- [43] K. V. Shanavas, D. Parker, and D. J. Singh, Theoretical study on the role of dynamics on the unusual magnetic properties in MnBi, *Sci. Rep.* **4**, 7222 (2014).
- [44] G. Pokharel, A. F. May, D. S. Parker, S. Calder, G. Ehlers, A. Huq, S. A. J. Kimber, H. S. Arachchige, L. Poudel, M. A. McGuire, D. Mandrus, and A. D. Christianson, Negative thermal expansion and magnetoelastic coupling in the breathing pyrochlore lattice material LiGaCr<sub>4</sub>S<sub>8</sub>, *Phys. Rev. B* **97**, 134117 (2018).
- [45] C. Hess, C. Baumann, U. Ammerahl, B. Büchner, F. Heidrich-Meisner, W. Brenig, and A. Revcolevschi, Magnon heat transport in (Sr, Ca, La)<sub>14</sub>Cu<sub>24</sub>O<sub>41</sub>, *Phys. Rev. B* **64**, 184305 (2001).
- [46] R. Baral, J. A. Christensen, P. K. Hamilton, F. Ye, K. Chesnel, T. D. Sparks, R. Ward, J. Yan, M. A. McGuire, M. E. Manley, J. B. Staunton, R. P. Hermann, and B. A. Frandsen, Real-space visualization of short-range antiferromagnetic correlations in a magnetically enhanced thermoelectric, *Matter* **5**, 1853 (2022).
- [47] M. E. Fisher, The renormalization group in the theory of critical behavior, *Rev. Mod. Phys.* **46**, 597 (1974).
- [48] A. D. Hillier, S. J. Blundell, I. McKenzie, I. Umegaki, L. Shu, J. A. Wright, T. Prokscha, F. Bert, K. Shimomura, A. Berlie, H. Alberto, and I. Watanabe, Muon spin spectroscopy, *Nat. Rev. Methods Primers* **2**, 4 (2022).
- [49] <https://www.energy.gov/doe-public-access-plan>.
- [50] Raw data of the neutron scattering experiments presented in this work can be accessed at: <https://doi.org/10.14461/oncat.data/2373061>.